

Article

A Novel Porous Ceramic Membrane Supported Monolithic Cu-Doped Mn–Ce Catalysts for Benzene Combustion

Zhaxi Cuo ^{1,2}, Dongdong Wang ^{1,2}, Yan Gong ^{1,2}, Feng Zhao ^{1,2} , Haidi Liu ¹ and Yunfa Chen ^{1,2,3,*}

¹ State Key Laboratory of Multi-phase Complex Systems, Institute of Process Engineering, Chinese Academy of Sciences, Beijing 100190, China

² University of Chinese Academy of Sciences, No. 19A Yuquan Road, Beijing 100049, China

³ CAS Center for Excellence in Urban Atmospheric Environment, Xiamen 361021, China

* Correspondence: chenyf@ipe.ac.cn; Tel.: +86-10-82544896; Fax: +86-10-62525716

Received: 10 July 2019; Accepted: 26 July 2019; Published: 30 July 2019



Abstract: Porous ceramic membranes (PCMs) are considered as an efficient hot gas filtration material in industrial systems. Functionalization of the PCMs with high-efficiency catalysts for the abatement of volatile organic compounds (VOCs) during dust elimination is a promising way to purify the industrial exhaust gases. In this work, we prepared PCMs (porosity: 70%) in a facile sintering process and integrated Cu-doped Mn–Ce oxides into the PCMs as monolithic catalysts by the sol–gel method for benzene oxidation. Through this method, the catalysts are dispersed evenly throughout the PCMs with excellent adhesion, and the catalytic PCMs provided more active sites for the reactant gases during the catalytic reaction process compared to the powder catalysts. The physicochemical properties of PCMs and catalytic PCMs were characterized systematically, and the catalytic activities were measured in total oxidation of benzene. As a result, all the prepared catalytic PCMs exhibited high catalytic activity for benzene oxidation. Significantly, the monolithic catalyst of Cu_{0.2}Mn_{0.6}Ce_{0.2}/PCMs obtained the lowest temperature for benzene conversion efficiency of 90% (T₉₀) at 212 °C with a high gaseous hourly space velocity of 5000 h^{−1} and showed strong resistance to high humidity (90 vol.%, 20 °C) with long-term stability in continuous benzene stream, which is caused by abundant active adsorbed oxygen, more surficial oxygen vacancy, and lower-temperature reducibility.

Keywords: ceramic membranes; monolithic catalyst; Cu-doped Mn–Ce oxides; benzene combustion; synergistic effect

1. Introduction

In recent years, air pollution, particularly the fine particulate matters (PM_{2.5}), has aroused general concern in China [1–4]. Diverse industrial processes and the ignition of non-renewable energy sources produce different kinds of volatile organic compounds (VOCs) containing PM_{2.5} which cause serious toxicological and unexpected side effects on the urban air quality, human body, and even on the climatic condition as secondary pollutants [5,6]. Generally, the effective filter materials of porous ceramic membranes (PCMs) were broadly utilized for PMs filtration owing to its unique properties, such as low density, high open porosity, high strength and toughness, incredible high temperature, and chemical resistance in the hot gas filtration processes [7–10]. In our pervious works, we prepared such filter materials successfully and received great PMs filtration efficiency under a lower pressure drop [11,12]. In fact, it is profoundly desirable to remove hazardous VOCs while we filter the PMs utilizing the PCMs from the hot gases simultaneously. For eliminating VOCs emissions, the catalytic oxidation is regarded as a compelling strategy compared to other VOCs disposal techniques, attributable to its

higher conversion efficiency at lower temperature [13–16]. A successful catalyst used for industrial applications usually requires high activity, stability, heat resistance, and low pressure drop during long-term operation for high airflow gaseous catalytic combustion. Therefore, a monolithic catalyst by functionalizing the PCMs with catalytic active ingredients is much necessary for the removal of VOCs during dedusting for air pollution control in the industrial application.

Currently, the transition metal oxide catalysts, by considering economical and effective elements, are better alternatives in contrast to the noble metal catalysts [17,18]. Among all the transition metals, the synergistic effect of Mn and Ce mixed oxides exhibited enhanced catalytic activity during benzene oxidation [19–23] that generally attributed to the abundance, low cost, numerous oxidation states, and high poison-resistance of manganese oxides [24,25], and the super oxygen storage capacity of ceria oxides which are regarded as viable segments in the VOCs oxidation [26,27]. Moreover, to further improve physiochemical properties, the ternary metal oxides catalysts (e.g., Mn–Ce–Co [28,29], Mn–Ce–Zr [30], Mn–Ce–Cu [31–33],) are popularly used in the field of VOCs removal. Such series of catalysts exhibit higher catalytic activity than binary and single metal oxides and show excellent stability and water vapor resistance properties during a long-term reaction due to the synergistic effects. The ionic radius of Cu is between the ionic radius of Mn and Ce, so the Cu ions can incorporate into the crystal lattice of Ce and Mn oxides. The doping of Cu species can promote the formation of more lattice defects and oxygen vacancies which improves the catalytic properties [34,35]. Hence, Cu-doped Mn–Ce ternary metal oxides catalyst system was chosen for benzene oxidation in this work.

Compared to conventional pellets or powder catalysts, the monolithic catalysts have numerous points of interest in mass and heat transfer, and can be characterized as a micro-flow reactor [36,37]. Herein, so as to functionalize the PCMs with high-efficient of catalytic capability for the industrial use and practical applications, we investigated a facile method to integrate the Cu-doped Mn–Ce catalysts into the fibrous PCMs for benzene (as target VOCs) oxidation. The sol–gel process has favorable advantages for the dispersion and adhesive strength between the catalysts and the supports compared to other techniques. Therefore, a sequence of monolithic Cu-doped Mn–Ce/PCMs catalysts were fabricated through the sol–gel method. Then, the impacts of copper doping content on VOCs catalytic conversion over monolithic catalysts were investigated through long-term benzene combustion. Subsequently, the physiochemical properties of samples were analyzed by using specific analysis techniques.

2. Results

Catalytic Activity for Benzene Combustion

We evaluated the catalytic performances of the synthesized monolithic catalysts for benzene oxidation in the reaction temperature range from 100 °C to 300 °C as shown in Figure 1. Throughout the measuring process, the CO₂ selectivity was always more than 98.0%, and there were no other products of incomplete oxidation detected, suggesting that the degree of catalytic oxidation is almost complete in the reaction. As a result, the amount of Cu doping has a great effect on the catalytic performance of Cu-doped Mn–Ce catalyst. The 10% Cu-doped Mn–Ce/PCMs sample showed better performance than Mn–Ce/PCMs in benzene catalytic oxidation, reaching 90% benzene conversion at 230 °C (T₉₀). As shown in Figure 1a, at first, the catalytic efficiency increased with the Cu doping content, and the catalytic activity of Mn_{0.6}Ce_{0.2}Cu_{0.2}/PCMs was better than other catalysts achieving 100% benzene conversion efficiency at 250 °C, and the T₉₀ was as low as 212 °C which was obviously lower than those obtained by the Mn–Ce catalyst. As Cu doping content kept rising, the catalytic performance began to drop. The detail reaction temperature at 50% (T₅₀) and 90% (T₉₀) benzene conversion of Mn–Ce/PCMs and series of Cu-doped Mn–Ce/PCMs catalysts are listed in Table 1. The results indicated that a small amount of Cu species can significantly improve the catalytic activity, and 20% Cu doping is a suitable content. To examine the stability and humidity resistance of the Mn_{0.6}Ce_{0.2}Cu_{0.2}/PCMs, the on-stream reaction of benzene oxidation over catalyst at 225 °C with 90 vol.% (20 °C) water vapor was conducted. As is shown in Figure 1b, Mn_{0.6}Ce_{0.2}Cu_{0.2}/PCMs exhibit high stability in the presence of high humidity

that a certain amount of water vapor has almost no effect on the activity of the catalyst. The texture properties of as-prepared catalysts and the mechanism discussions are illustrated in the following text.

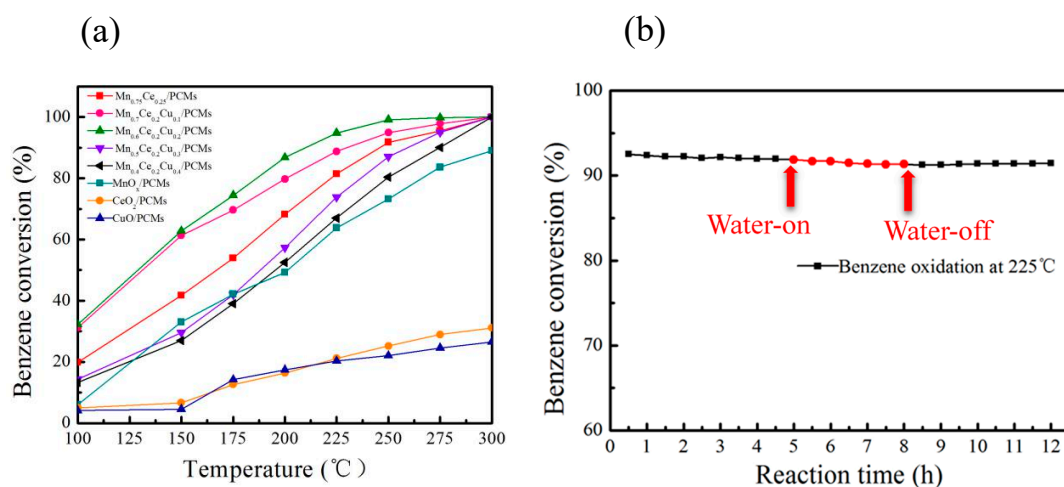


Figure 1. (a) Benzene conversion as a function of reaction temperature over various catalytic porous ceramic membranes (PCMs) (100 ppm of benzene, synthetic air balance, gaseous hourly space velocity (GHSV) of 5000 h⁻¹). (b) Effect of water vapor on the activity of Mn_{0.6}Ce_{0.2}Cu_{0.2}/PCMs at 225 °C.

Table 1. Textural properties, catalytic activities, X-ray photoelectron spectroscopy (XPS) analysis, and cumulative H₂ consumption in hydrogen temperature-programmed reduction (H₂-TPR) of the Mn–Ce/PCMs and Cu-doped Mn–Ce/PCMs catalysts with different Cu doping content.

| Catalysts | BET (m ² /g) | Total Pore Volume D _v (cc/g) | Average Pore Size D _p (nm) | T ₅₀ (°C) | T ₉₀ (°C) | Ce ³⁺ /(Ce ³⁺ +Ce ⁴⁺) | Mn ⁴⁺ /Mn ³⁺ | (O _{ads})/O | H ₂ Consumption (mmol/g) |
|---|-------------------------|---|---------------------------------------|----------------------|----------------------|---|------------------------------------|-----------------------|-------------------------------------|
| Mn _{0.75} Ce _{0.25} /PCMs | 22.1 | 0.089 | 6.08 | 165 | 246 | 0.153 | 0.858 | 1.119 | 1.285 |
| Mn _{0.7} Ce _{0.2} Cu _{0.1} /PCMs | 29.7 | 0.091 | 6.18 | 135 | 230 | 0.196 | 0.903 | 1.958 | 1.902 |
| Mn _{0.6} Ce _{0.2} Cu _{0.2} /PCM | 29.5 | 0.084 | 7.58 | 130 | 212 | 0.225 | 1.177 | 2.201 | 1.974 |
| Mn _{0.5} Ce _{0.2} Cu _{0.3} /PCMs | 14.0 | 0.070 | 9.67 | 185 | 260 | 0.204 | 0.860 | 1.146 | 1.733 |
| Mn _{0.4} Ce _{0.2} Cu _{0.4} /PCMs | 13.5 | 0.066 | 9.73 | 195 | 276 | 0.196 | 0.788 | 1.051 | 1.503 |

3. Discussion

3.1. Phase Characterization and Textural Properties

The prepared PCMs showed high porosity (apparent porosity 70%), high compressive strength (5.5 Mpa), low density (0.88 g/cm³), low linear shrinkage (lower than 0.5%), and excellent corrosion resistance in a strong acid or base solution, which is applicable for the environment that is even associated with high-temperature or chemical corrosive conditions. The phase analysis of calcined support PCMs and the PCMs with different loadings of Mn, Ce, and Cu species was evaluated by X-ray diffraction (XRD). The results in Figure 2 showed strong diffraction mullite peaks [3Al₂O₃ 2SiO₂, PDF #00-015-0776] and low-intensity cristobalite peaks [SiO₂, PDF #01-082-1233] which were attributed to the PCMs support. The relatively weak peaks of manganese oxides (MnO₂, PDF#01-072-1983 and Mn₃O₄, PDF#03-065-2776), the cerium oxide (CeO₂, PDF#00-044-1001) can be detected from all catalytic PCMs; copper oxide (CuO, PDF#01-089-2530) phases were detected in the Cu doped Mn–Ce/PCMs catalysts. The XRD data showed that Cu-doped Mn–Ce oxides were integrated into the PCMs as monolithic catalysts. Moreover, the weak diffraction peaks of Cu–Mn oxides including (Cu_{1.5}Mn_{1.5}O₄, PDF#01-070-0262) and (CuMn₂O₄, PDF#01-074-1919) were observed in the Cu-doped Mn–Ce/PCMs. It can be deduced that Cu ion doping distorted the crystal lattice of MnO_x slightly. Meanwhile, another weak diffraction peak of ceria copper oxide (Cu_xCe_{1-x}O₂, PDF#01-070-0262) was detected, which showed copper ions were also partially incorporated into the CeO₂ crystal lattice and formed the relevant solid solution. Therefore, compared to MnO_x/PCMs, CeO₂/PCMs, and Mn–Ce/PCMs catalysts,

the Cu-doped Mn–Ce/PCMs catalysts showed more lattice defects and active sites which promote the electron or oxygen transfer due to the synergistic effects between the Mn–Ce oxides and Cu element.

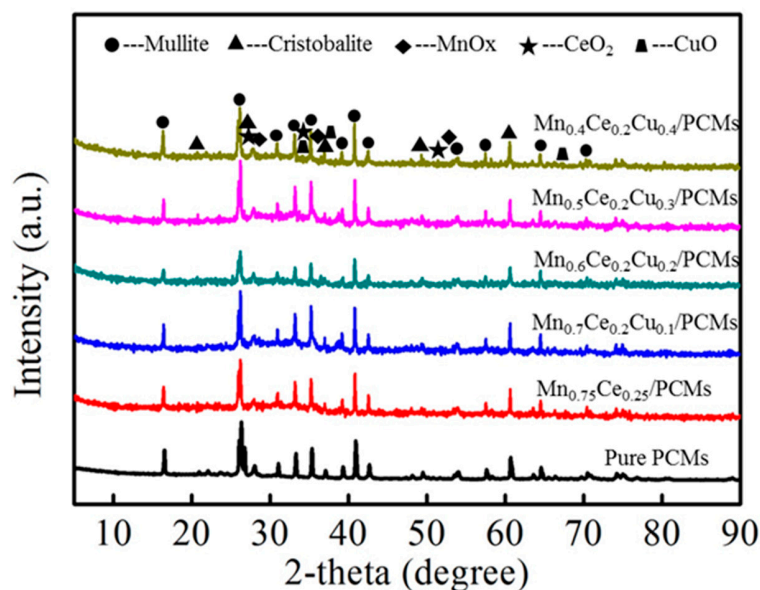


Figure 2. X-ray diffraction (XRD) patterns of the support PCMs and catalytic PCMs with different Cu, Mn, and Ce ratio.

The optical images of PCMs before and after supported catalysts are shown in Figure 3a. The surface of support PCMs was regular and flat without any apparent holes or flaws. The PCMs after supported catalysts showed an obvious color change from white to black. The active oxides exhibited great adhesion to the PCMs support after calcination. The amount of catalyst grown on the PCMs ($4.250 \pm 0.2\text{g}$) were about $30 \pm 1\text{wt.}\%$ loadings which included different Cu, Mn, and Ce atomic ratios. The as-prepared monolithic catalysts were defined as a micro-flow reactor which can improve gas and heat transfer during reaction processes.

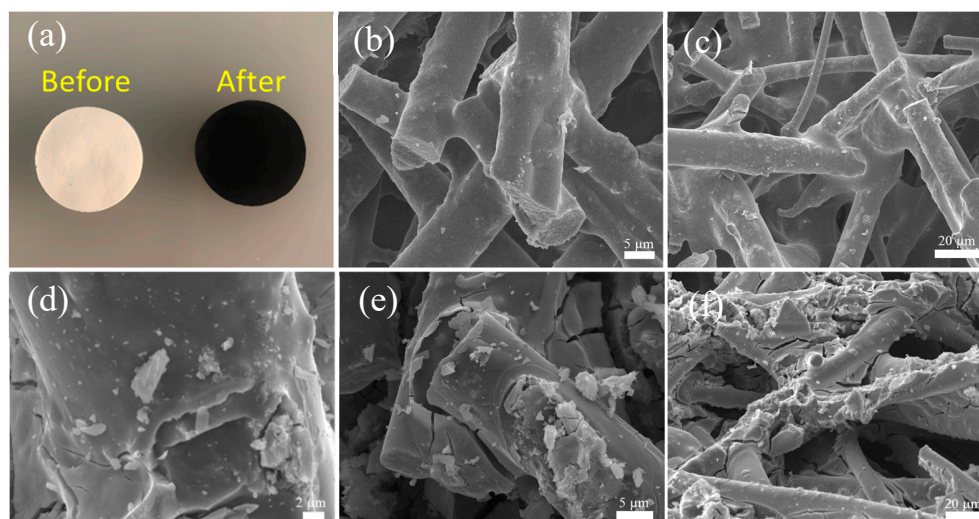


Figure 3. Optical image of the PCMs samples before and after the catalyst incorporation (a); microstructure before (b,c) and after (d–f) the catalyst incorporation.

The microstructure of the samples was observed by scanning electron microscope (SEM) as shown in Figure 3b–f. The PCMs showed a specifically high porous network structure, and the catalyst active components were homogeneously coated in the skeleton of the PCMs. The element content

and dispersion of samples were examined by scanning electron microscopy–energy dispersive X-ray spectrometry (SEM–EDS) analysis. Figure 4 shows the SEM–EDS analysis of $\text{Mn}_{0.6}\text{Ce}_{0.2}\text{Cu}_{0.2}/\text{PCMs}$ as an example. The atomic ratio of Cu and Mn/Ce was close to the initial metal salt solution, and the catalyst particles were uniformly distributed in the three-dimensional network structure of the PCMs.

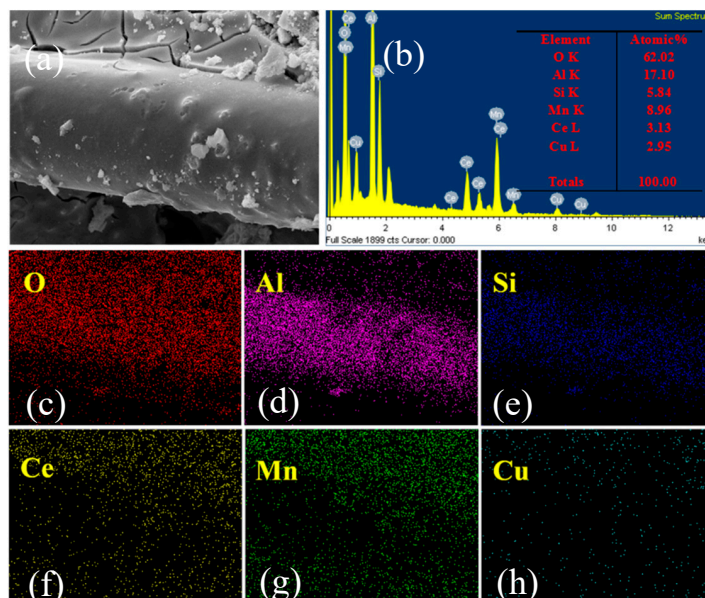


Figure 4. Scanning electron microscopy–energy dispersive X-ray spectrometry (SEM–EDS). (a) SEM photo of scan area; (b) element content; (c–h) surface elemental mapping images of $\text{Mn}_{0.6}\text{Ce}_{0.2}\text{Cu}_{0.2}/\text{PCMs}$.

To evaluate the changes of pore structure, the pore size distributions of the support PCMs and catalytic PCMs were analyzed by mercury intrusion method. All the catalytic samples showed similar results; here we take $\text{Mn}_{0.6}\text{Ce}_{0.2}\text{Cu}_{0.2}/\text{PCMs}$ as an example. As shown in Figure 5, the PCMs demonstrated a narrow pores size distribution condition. The pore distribution of support PCMs ranged from 10 to 50 μm , and the most probable distribution appeared at about 26.4 μm . Accordingly, compared to support PCMs, the main pore size of PCMs with loading catalysts (mainly appeared at 24.5 μm) showed slight changes, but the pore size distribution was between 10–60 μm , which is quite close to the support PCMs.

The transmission electron microscopy (TEM) and high-resolution transmission electron microscopy (HRTEM) images of Cu-doped Mn–Ce oxide, Mn–Ce oxide pure CeO_2 , MnO_x catalysts supported onto the PCMs were analyzed as shown in Figure 6. Figure 6a–d indicate that the active components of the catalysts were composed of tiny particles with a loose surface. From the HRTEM images (Figure 6e) of the CeO_2 catalyst, the surface lattice spacing with 0.421 nm distance is assigned to (110) crystal plane of CeO_2 phase. The lattice fringes with 0.308 nm and 0.323 nm (Figure 6f) are corresponding to the lattice planes of Mn_3O_4 (202) and MnO_2 (210), respectively. The HRTEM image of the Mn–Ce oxides catalyst (Figure 6g) reveals two identified fringes with about 0.322 nm and 0.215 nm which can be assigned to (210) crystal phase of MnO_2 and (213) phase of CeO_2 . For Cu-doped Mn–Ce oxides (Figure 6h), the measured lattice spacing with 0.421 nm, 0.278 nm, and 0.243 nm distances are assigned to the lattice planes of CeO_2 (110) with good crystallization, the (110) CuO plane with slightly poor crystallization, and MnO_2 (201) phase, respectively. The TEM results demonstrate that the lattice planes of MnO_x and CeO_2 are changed with the Cu incorporation, which is in agreement with the discussions in the XRD analysis.

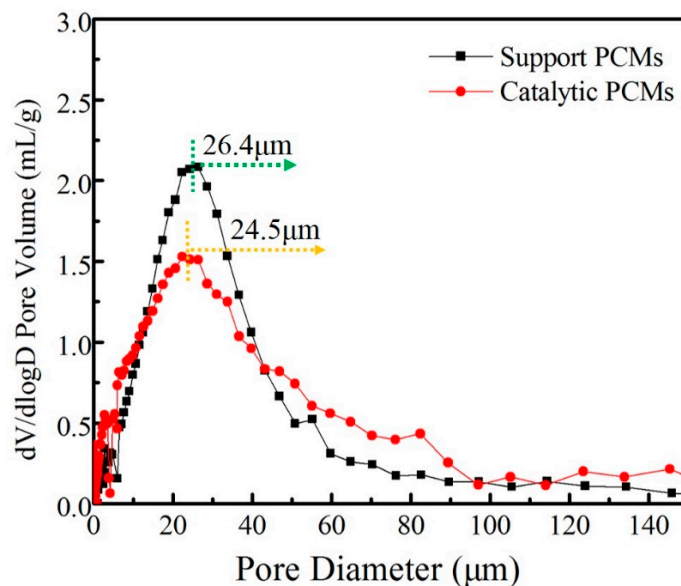


Figure 5. The pore size distributions of support PCMs and catalytic PCMs.

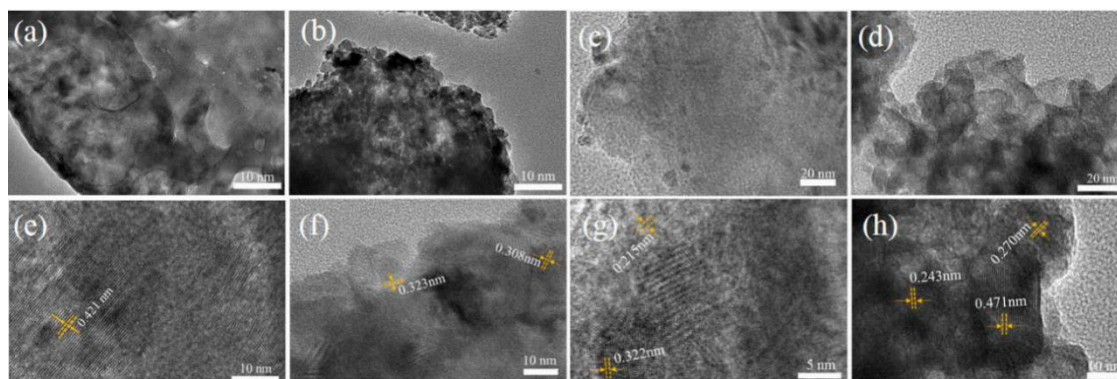


Figure 6. Transmission electron microscopy (TEM) images of the CeO_2 , MnO_x , Mn–Ce oxides and Cu-doped Mn–Ce oxides samples (a–d) supported onto the PCMs; the high-resolution transmission electron microscopy (HR TEM) images (e–h) corresponding to (a–d), respectively.

3.2. N_2 Adsorption–Desorption Analysis

The specific surface area (S_{BET}), average pore size (D_p), and total pore volume (D_V) of support PCMs and catalytic PCMs are shown in Table 1. The S_{BET} of all catalyst-supported PCMs were higher than that of pure PCMs ($3.3 \text{ m}^2/\text{g}$). When Cu species were partially incorporated into the Mn and Ce oxides, the samples showed larger surface areas around $29.5\text{--}29.7 \text{ m}^2/\text{g}$ for $\text{Mn}_{0.7}\text{Ce}_{0.2}\text{Cu}_{0.1}/\text{PCMs}$ and $\text{Mn}_{0.6}\text{Ce}_{0.2}\text{Cu}_{0.2}/\text{PCMs}$ catalysts compared with that of Mn–Ce catalysts (about $22.1 \text{ m}^2/\text{g}$). However, the S_{BET} of the $\text{Mn}_{0.5}\text{Ce}_{0.2}\text{Cu}_{0.3}/\text{PCMs}$ ($14.1 \text{ m}^2/\text{g}$) and $\text{Mn}_{0.4}\text{Ce}_{0.2}\text{Cu}_{0.4}/\text{PCMs}$ ($13.5 \text{ m}^2/\text{g}$) catalysts decreased with the continuous decrease in the manganese content. Furthermore, the average pore size became larger for Cu-doped catalysts with $7.58\text{--}9.73 \text{ nm}$ than those samples without Cu incorporation. The results revealed that Cu doping into the Mn and Ce species leads to change in the catalyst surface structures.

3.3. X-ray Photoelectron Spectra

Figure 7 shows XPS spectra of the Mn 2p, Ce 3d, Cu 2p, and O 1s of the samples. From Figure 7a, the Mn 2p XPS spectra for binding energies of Mn $2p_{3/2}$ and Mn $2p_{1/2}$ are consistent with the previous reported results [21,38]. The Mn $2p_{3/2}$ peaks can be divided into three components located at BE = 641.2, 642.5, and 644.3 eV attributed to the surface Mn^{3+} , Mn^{4+} , and the satellite peak of Mn^{3+} , respectively.

The atomic ratios of $\text{Mn}^{4+}/\text{Mn}^{3+}$ were calculated from the peak areas of XPS spectra as listed in Table 1. Apparently, the Cu doping content has an obvious influence on the surface $\text{Mn}^{4+}/\text{Mn}^{3+}$ ratios. When Cu species are incorporated into the Mn–Ce crystal lattices, the $\text{Mn}^{4+}/\text{Mn}^{3+}$ atomic ratios increased. The higher value manganese oxidation state (Mn^{4+}) possesses more oxygen vacancy in the MnO_x crystal lattice, which introduce more surface positive charge that is beneficial for the formation of adsorbed oxygen. Meanwhile, the presence of a small amount of lower value manganese state (Mn^{3+}) in the crystal produces oxygen vacancies and promote the lattice oxygen migration [39]. The $\text{Mn}^{4+}/\text{Mn}^{3+}$ ratios of catalysts follow the order below: $\text{Mn}_{0.6}\text{Ce}_{0.2}\text{Cu}_{0.2}/\text{PCMs} > \text{Mn}_{0.7}\text{Ce}_{0.2}\text{Cu}_{0.1}/\text{PCMs} > \text{Mn}_{0.5}\text{Ce}_{0.2}\text{Cu}_{0.3} > \text{Mn}_{0.75}\text{Ce}_{0.25}/\text{PCMs}/\text{PCMs} > \text{Mn}_{0.4}\text{Ce}_{0.2}\text{Cu}_{0.4}/\text{PCMs}$. As shown in Figure 7b, The XPS spectra of Ce 3d are separated into eight peaks, and the peaks marked v and u represent the spin-orbit doublets of Ce $3d_{5/2}$ and Ce $3d_{3/2}$, respectively. The peaks located at BE = 884.9 eV (v_1) and 901.0 eV (u_1) are assigned to the Ce^{3+} species, while the Ce^{4+} is characterized by six other peaks: BE = 882.7 eV (v_0), 888.9 eV (v_2), 898.5 eV (v_3), 903.2 eV (u_0), 907.3 eV (u_2), and 916.8 eV (u_3) [21,40]. The results showed that both Ce^{4+} and Ce^{3+} states existed in all the catalysts, and the Ce species mainly existed in Ce^{4+} oxidation state. However, the existence of small amount of Ce^{3+} , which can lose an electron to get oxidized to Ce^{4+} in the catalysts, therefore improves the redox transformation process [41]. Table 1 also summarizes the ratio of Ce^{3+} to total Ce results calculated from the XPS spectra. The catalyst of $\text{Mn}_{0.6}\text{Ce}_{0.2}\text{Cu}_{0.2}/\text{PCMs}$ exhibits the highest amount of Ce^{3+}/Ce (0.225) of all the catalysts.

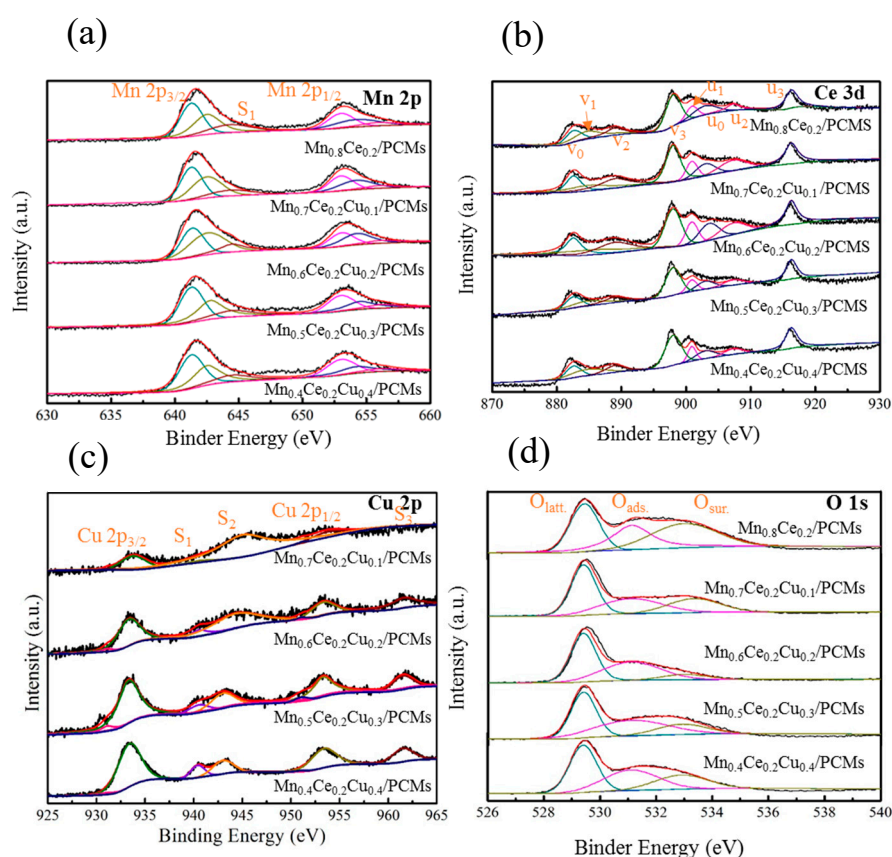


Figure 7. XPS spectra of the (a) Mn 2p, (b) Ce 3d, (c) Cu 2p, and (d) O 1s of the catalysts.

The Cu 2p XPS spectra of the samples are presented in Figure 7c. XPS spectra of $\text{Mn}_{0.7}\text{Ce}_{0.2}\text{Cu}_{0.1}/\text{PCMs}$ is disordered which is caused by the low content of Cu species. All the Cu 2p XPS spectra are characterized by two primary areas of Cu $2p_{1/2}$ and Cu $2p_{3/2}$ accompanying with shake-up satellite peaks. The Cu $2p_{3/2}$ peaks located at BE = 933.3 eV and Cu $2p_{1/2}$ at BE = 953.3 eV with a strong shake-up satellite at BE = 940–945 eV (remarked as S_1 and S_2) are recognized

as Cu^{2+} . Another relatively weak Cu $2p_{3/2}$ peak at 931.1 eV and Cu $2p_{1/2}$ at 951.1 eV is observed for the high Cu containing catalysts that can be due to the Cu^+ ions [42,43]. The O 1s XPS spectra of the samples can be broken down to three components as shown in Figure 7d. Respectively, the peaks at 529.6 eV are for surface lattice oxygen (O_{latt} , O^{2-}), 531.7 eV for the adsorbed oxygen (O_{ads} , O_2^- , O^{2-} , O^-), and 532.7 eV for the adsorbed OH groups (O_{sur}) [44]. According to the electroneutrality principle, more adsorbed oxygen species are formed by increasing the higher manganese oxidation state (Mn^{4+}) content [39]. Compared to the Mn–Ce/PCMs catalyst, Cu-doped Mn–Ce/PCMs catalysts have more O_{ads} (as listed in Table 1). The adsorbed oxygen also can be promoted by the “Cu←O” electron-transfer process [45,46]. The catalyst of $\text{Mn}_{0.6}\text{Ce}_{0.2}\text{Cu}_{0.2}$ /PCMs with the most (O_{ads})/O ratio (0.201) showed the best catalytic performance during oxidation of benzene.

3.4. H_2 -TPR Analysis

The reduction of the prepared monolithic catalysts with different amounts of Cu ions was carried out by H_2 -TPR. The support PCMs are difficult to be reduced due to their strong thermal and chemical stability, so the reduction peaks belong to the reduction of Cu–Mn–Ce oxides during the test procedure. As shown in Figure 8, each H_2 -TPR result of Cu-doped mixed catalysts showed two reduction peaks at below 300 °C. The incorporation of Cu species into the catalysts can mutually facilitate the reduction of each active component, therefore all the reduction peaks are difficult to distinguish owing to the higher reducibility of Cu [47,48]. From Figure 8, the reduction peaks at low temperature is attributed to the highly dispersed Cu ions, while the high temperature peaks can be due to the reduction of Cu^+ species [49,50], and Table 1 also listed the H_2 -consumptions of each reduction peaks in TPR profiles. The result shows that temperature of reduction peaks slightly shift to lower temperature zone and its H_2 consumption is obviously increased with the addition of Cu species and indicates a strong interaction between the Cu and Mn–Ce oxides. The $\text{Mn}_{0.6}\text{Ce}_{0.2}\text{Cu}_{0.2}$ /PCMs achieves the best reducibility showing the most H_2 consumption (1.974 mmol/g) with the maximum amount estimated for the elements in their highest oxidation state. A possible explanation is that the Cu reduction occurs with the reduction of Mn and Ce ions, and doping Cu species obviously improved the content of lattice defect and oxygen vacancies which results in enhanced mobility of active oxygen species. The promoted oxygen mobility of the as-prepared catalysts will be beneficial to the oxidation of benzene.

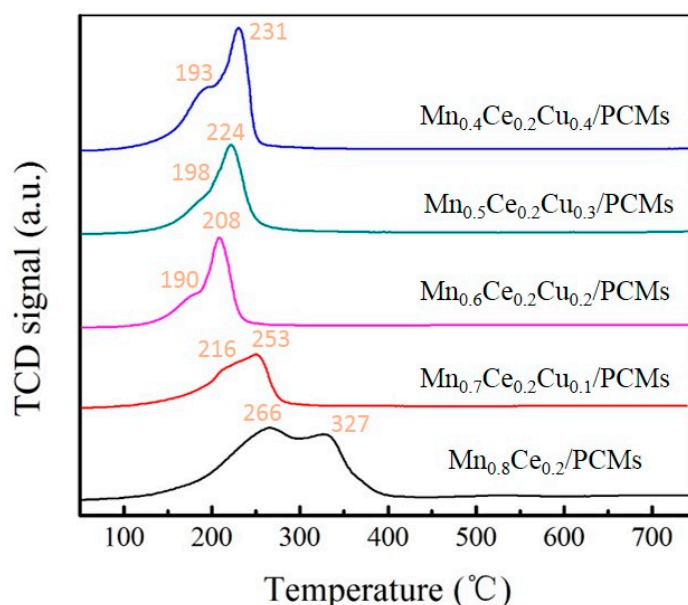


Figure 8. H_2 -TPR profiles of catalysts with different Cu doping content.

3.5. Proposed Benzene Oxidation Mechanism

According to the above characterization results, the proposed benzene oxidation mechanism of Cu-doped Mn–Ce monolithic catalyst is discussed. Figure 9 demonstrates the possible route for benzene catalytic oxidation over the Cu-doped Mn–Ce/PCMs catalyst. PCMs were fabricated by linking mullite fibers with different kinds of addition agents in a sinter-locked three-dimensional structure under high temperature treatment. By loading catalytic components to the ceramic membrane, a monolithic structured catalyst with their unique properties can be obtained. The as-prepared PCMs is a novel catalyst support which can effectively improve the gas and heat transfer during the reaction process. After integrating the Cu-doped Mn–Ce oxides into the PCMs as monolithic catalysts, the $\text{Mn}_{0.6}\text{Ce}_{0.2}\text{Cu}_{0.2}/\text{PCMs}$ shows significant catalytic activity. According to the XRD patterns, weak peaks of copper manganese oxide ($\text{Cu}_{1.5}\text{Mn}_{1.5}\text{O}_4$, CuMn_2O_4) and ceria copper oxide ($\text{Cu}_x\text{Ce}_{1-x}\text{O}_2$) were detected over the Cu-doped Mn–Ce/PCMs, indicating the influence of the introduced Cu ion on the crystal lattice of Mn–Ce oxides and the great synergistic interaction between the Cu and Mn–Ce species, and the relevant analysis in TEM intuitively demonstrated the corresponding results as well. The discussions from H_2 -TPR and XPS analysis confirmed the improved reducibility and abundance of active adsorbed oxygen generated on the $\text{Mn}_{0.6}\text{Ce}_{0.2}\text{Cu}_{0.2}/\text{PCMs}$ interface. The adsorbed oxygen, which is critical for the high catalytic activity of $\text{Mn}_{0.6}\text{Ce}_{0.2}\text{Cu}_{0.2}/\text{PCMs}$ in the benzene oxidation, is promoted by the higher content of Mn^{4+} with Cu doping. The results demonstrated the electronic transfer between Mn, Ce, and Cu ions due to the following redox processes: $\text{Mn}^{4+} + \text{Ce}^{3+} \leftrightarrow \text{Mn}^{3+} + \text{Ce}^{4+}$, $\text{Mn}^{4+} + \text{Cu}^+ \leftrightarrow \text{Cu}^{2+} + \text{Mn}^{3+}$, $\text{Ce}^{4+} + \text{Cu}^+ \leftrightarrow \text{Cu}^{2+} + \text{Ce}^{3+}$. The redox transport processes can be beneficial for the catalytic reaction. In addition, the great catalytic performance of $\text{Mn}_{0.6}\text{Ce}_{0.2}\text{Cu}_{0.2}/\text{PCMs}$ for benzene oxidation may result from its stable and active interface structure, uniform distribution of surface species, high reducibility, high concentrations of active adsorbed oxygen, and oxygen vacancies.

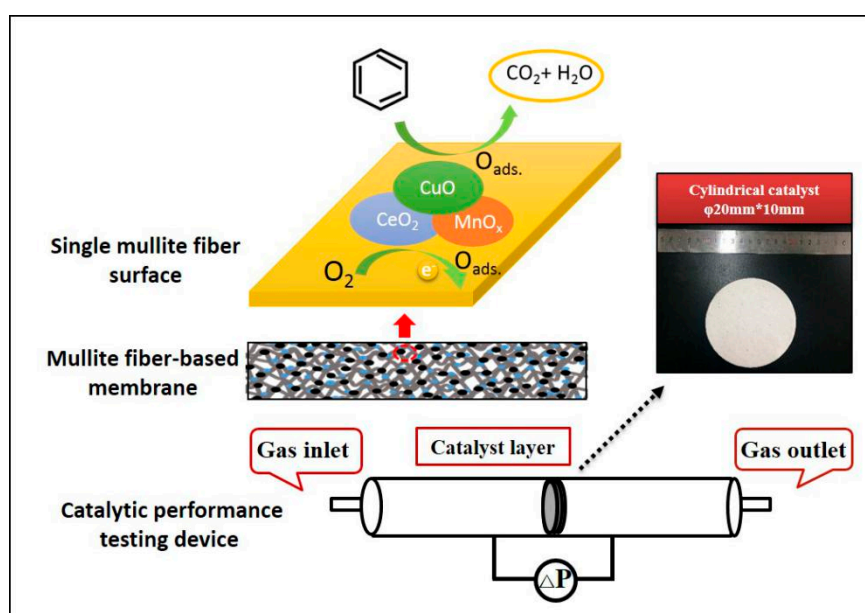


Figure 9. Schematic diagram of the catalytic performance testing device and the proposed benzene oxidation pathway over Cu-doped Mn–Ce/PCMs catalysts.

4. Materials and Methods

4.1. Preparation of PCMs and Catalytic PCMs

The original PCMs were prepared through molding method as detailed in our previous works [12,19]. In brief, a raw mixture containing short-cut mullite fiber, binder of kaolin and kaliaibite, carboxymethylcellulose, corn starch, as well as deionized water was ball-milled proportionally to

form the slurry. Then the green bodies of PCMs were manufactured by pressing a specific amount of mixture into a circular metal mold with a diameter of 50 mm at 2 Mpa. After drying (at 105 °C, 2 h) and sintering (at 1250 °C, 2 h, 3 °C/min) of the prepared samples, we finally obtained the support PCMs, and all the PCMs used for catalysts support were cut into cylindrical shape (Φ 20 mm \times 10 mm). At first, the small PCMs disks were immersed in concentrated nitric acid (10 wt.%) at room temperature for 12 h to remove soluble impurities, afterward, the treated PCMs were cleaned thoroughly with deionized water and then dried overnight at 120 °C.

The Mn–Ce/PCMs catalysts and different atomic ratio of Cu-doped Mn–Ce/PCMs were prepared by the sol–gel method as follows. First, $\text{Ce}(\text{NO}_3)_3 \cdot 6\text{H}_2\text{O}$, $\text{Mn}(\text{NO}_3)_2$ (50 wt.% aqueous solution), $\text{Cu}(\text{NO}_3)_2 \cdot 4\text{H}_2\text{O}$, and citric acid ($n_{\text{(citric acid)}}:n_{\text{(Mn + Ce + Cu)}} = 0.3$ in molar ratio) were mixed in proper molar ratios in an appropriate volume of deionized water to obtain a stable solution. Then the solution was stirred continuously at 80 °C for 4 h to produce a sol, and the cylindrical PCMs were dipped into this viscous solution for 2 h under stirring. Subsequently, the prepared samples were dried at 130 °C for 12 h and sintered at 550 °C for 4 h in the air. By this experimental procedure, uniform dispersed catalysts formed on the monolithic PCMs during heat treatment, and the total loading of catalysts per PCMs were 30 ± 1 wt.%. Thus, the monolithic catalysts with different atomic ratios (marked as $\text{Mn}_x\text{Ce}_y\text{Cu}_z/\text{PCMs}$ where x , y , and z are the molar ratios of Mn, Ce, Cu in the catalysts, respectively) based on the Cu-doped Mn–Ce/PCMs were prepared following the same schedule.

4.2. Characterization of PCMs and Catalytic PCMs

The microstructures of the samples were examined by scanning electron microscopy (SEM, JEOL, JSM-6700F, Tokyo, Japan) and transmission electron microscopy (TEM, JEOL, JEM-2100F, Tokyo, Japan). Energy dispersive X-ray spectrometer (EDS, EMAX-500, HORIBA Ltd., Tokyo, Japan) connected to a SEM was used to analyze the elemental mapping. The technique of mercury porosimetry (AutoPore IV 9500, Norcross, GA, USA) was applied to test the porosity and mainly the pore size distribution of the support PCMs. The crystal structure of samples was characterized via X-ray diffraction (XRD, PANalytical, X'Pert PRO MPD Cu $K\alpha = 1.542 \text{ \AA}$, The Netherlands). The specific surface area of the catalysts was measured by the Brunauer-Emmett-Teller (BET) method via N_2 adsorption and desorption method by the automatic surface analyzer (AS-1-C TCD, Quantachrome Cor., Boynton Beach, FL, USA). To analyze the reducibility performance of the catalysts, hydrogen temperature-programmed reduction (H_2 -TPR) was employed which operated with an automated catalyst characterization system (Autochem 2920, Micromeritics, Norcross, GA, USA). The surface species of catalysts were determined by X-ray photoelectron spectroscopy (XPS, XLESCAL AB 250Xi electron spectrometer, VG Scientific, Waltham, MA, USA).

4.3. Catalytic Performance Evaluation

The catalytic oxidation performances for benzene combustion were conducted in a fixed-bed quartz tubular microreactor (diameter 20 mm) at an atmospheric pressure using a gaseous hourly space velocity (GHSV) of 5000 h^{-1} . In each test, a cylindrical catalytic PCM (Φ 20 mm \times 10 mm) was loaded inside of the quartz tube reactor. The catalyst bed temperature was detected by a thermocouple placed in the heating furnace. The measured temperature ranged from 100 °C to 300 °C during the catalytic reaction. The reactant airflow was composed of 100 ppm benzene with synthetic air. The concentrations of C_6H_6 and CO_2 in the inlet and outlet gases were tested by a gas chromatograph (Shimadzu GC-2014) equipped with flame ionization detector (FID) and methanizer furnace. The catalytic performances of the samples were estimated based on benzene conversion and CO_2 yield which determined as follows:

Benzene conversion:

$$X_{\text{benzene}} = \frac{[\text{benzene}]_{\text{in}} - [\text{benzene}]_{\text{out}}}{[\text{benzene}]_{\text{in}}} \times 100\% \quad (1)$$

CO₂ yield:

$$\mu_{\text{CO}_2} = \frac{[\text{CO}_2]_{\text{in}}}{6 * [\text{benzene}]_{\text{in}}} \times 100\% \quad (2)$$

where [benzene]_{in}, [benzene]_{out} represent the benzene concentration (ppm) of inlet gas and outlet gas respectively. [CO₂]_{out} represents the CO₂ concentration (ppm) of the outlet gas. To analyze the influence of water vapor for the catalytic performance, we produced water vapor by bubbling water with air to bring in the on-stream benzene oxidation experiment, and a humidity sensor meter (center 310 RS-232, TES, Taipei, Taiwan) was employed to measure the corresponding relative humidity in the testing process.

5. Conclusions

In summary, we successfully fabricated porous ceramic membranes which served as a catalyst support. Then, Mn–Ce catalysts doped with varying Cu content were coated on the PCMs through sol–gel method. Hence, a highly efficient monolithic catalyst of Cu-doped Mn–Ce/PCMs was synthesized for the removal of VOCs, showing that Cu doping content has a great impact on the catalytic performance of the monolithic catalysts. The incorporation of Cu species effectively enhanced the catalytic activity compared to Mn–Ce bimetallic mixed oxides. Furthermore, among all samples, the as-prepared catalyst of Mn_{0.6}Ce_{0.2}Cu_{0.2}/PCMs showed the best catalytic activity for benzene oxidation with the lowest T₉₀ at 212 °C and a favorable stability under GHSV of 5000 h^{−1}. This activity is higher than other catalysts and the T₉₀ was 35 °C lower than those achieved over the Mn–Ce/PCMs catalyst. The enhanced catalytic activity caused by the formation of more oxygen vacancies and lattice defects brought by Cu doping in the surface of catalysts was due to the synergistic effects. In addition, the PCMs demonstrated a narrow pore distribution before and after the supporting catalysts, and the well-adhered catalysts were almost dispersed throughout the PCMs network structures homogeneously, ensuring high catalytic activity and stability under a low pressure drop. In all, our work demonstrates a promising way to functionalize the PCMs with high-efficient catalytic components as a monolithic catalyst for the removal of hazardous VOCs from industrial processes associated with harsh conditions such as high temperature and corrosive environments.

Author Contributions: Conceptualization, Z.C. and H.L.; methodology, Z.C., D.W., Y.G.; software, Z.C.; validation, Z.C., Y.G., and Y.C.; formal analysis, Z.C., D.W., and Y.G.; investigation, Z.C. and H.L.; resources, H.L. and Y.C.; data curation, Z.C. and F.Z.; writing—original draft preparation, Z.C.; writing—review and editing, Y.G. and F.Z.; supervision, Y.C.; funding acquisition, H.L. and Y.C.

Funding: This research was funded by the “Transformational Technologies for Clean Energy and Demonstration”, Strategic Priority Research Program of the Chinese Academy of Sciences (Grant No. XDA 210000000), the Key Deployment Program of the Chinese Academy of Sciences (Grant No. ZDRW-ZS-2017-6-2), and National Key R&D Program of China (Grant No. 2017YFC0702700).

Conflicts of Interest: The authors declare no conflict of interest.

References

1. Zou, B.B.; Huang, X.F.; Zhang, B.; Dai, J.; Zeng, L.W.; Feng, N.; He, L.Y. Source apportionment of PM_{2.5} pollution in an industrial city in southern China. *Atmos. Pollut. Res.* **2017**. [[CrossRef](#)]
2. He, Z.; Li, G.; Chen, J.; Huang, Y.; An, T.; Zhang, C. Pollution characteristics and health risk assessment of volatile organic compounds emitted from different plastic solid waste recycling workshops. *Environ. Int.* **2015**, *77*, 85–94. [[CrossRef](#)] [[PubMed](#)]
3. Liu, B.; Song, N.; Dai, Q.; Mei, R.; Sui, B.; Bi, X.; Feng, Y. Chemical composition and source apportionment of ambient PM_{2.5} during the non-heating period in Taian, China. *Atmos. Res.* **2016**, *170*, 23–33. [[CrossRef](#)]
4. Ma, Q.; Cai, S.; Wang, S.; Zhao, B.; Martin, R.V.; Brauer, M.; Cohen, A.; Jiang, J.; Zhou, W.; Hao, J.; et al. Impacts of coal burning on ambient PM_{2.5} pollution in China. *Atmos. Chem. Phys.* **2017**, *17*, 4477–4491. [[CrossRef](#)]

5. Kamal, M.S.; Razzak, S.A.; Hossain, M.M. Catalytic oxidation of volatile organic compounds (VOCs)—A review. *Atmos. Environ.* **2016**, *140*, 117–134. [[CrossRef](#)]
6. Luengas, A.; Barona, A.; Hort, C.; Gallastegui, G.; Platel, V.; Elias, A. A review of indoor air treatment technologies. *Rev. Environ. Sci. Bio. Technol.* **2015**, *14*, 499–522. [[CrossRef](#)]
7. Yang, Y.; Xu, W.; Zhang, F.; Low, Z.X.; Zhong, Z.; Xing, W. Preparation of highly stable porous SiC membrane supports with enhanced air purification performance by recycling NaA zeolite residue. *J. Membr. Sci.* **2017**, *541*, 500–509. [[CrossRef](#)]
8. Lupion, M.; Alonso-Fariñas, B.; Rodriguez-Galan, M.; Navarrete, B. Modelling pressure drop evolution on high temperature filters. *Chem. Eng. Process. Process Intensif.* **2013**, *66*, 12–19. [[CrossRef](#)]
9. Karmakar, M.K.; Chandra, P.; Chatterjee, P.K. A review on the fuel gas cleaning technologies in gasification process. *J. Environ. Chem. Eng.* **2015**, *3*, 689–702. [[CrossRef](#)]
10. Das, B.; Chakrabarty, B.; Barkakati, P. Preparation and characterization of novel ceramic membranes for micro-filtration applications. *Ceram. Int.* **2016**, *42*, 14326–14333. [[CrossRef](#)]
11. Cuo, Z.; Liu, H.; Zhao, F.; Li, W.; Peng, S.; Chen, Y. Highly porous fibrous mullite ceramic membrane with interconnected pores for high performance dust removal. *Ceram. Int.* **2018**. [[CrossRef](#)]
12. Cuo, Z.; Zhang, J.; Yu, B.; Peng, S.; Liu, H.; Chen, Y. Spherical Al₂O₃-coated mullite fibrous ceramic membrane and its applications to high-efficiency gas filtration. *Sep. Purif. Technol.* **2019**, *215*, 368–377. [[CrossRef](#)]
13. Tomatis, M.; Xu, H.-H.; He, J.; Zhang, X.-D. Recent Development of Catalysts for Removal of Volatile Organic Compounds in Flue Gas by Combustion: A Review. *J. Chem.* **2016**, *2016*, 1–15. [[CrossRef](#)]
14. Zhang, Z.; Jiang, Z.; Shangguan, W. Low-temperature catalysis for VOCs removal in technology and application: A state-of-the-art review. *Catal. Today* **2016**, *264*, 270–278. [[CrossRef](#)]
15. Yao, X.; Tang, C.; Gao, F.; Dong, L. Research progress on the catalytic elimination of atmospheric molecular contaminants over supported metal-oxide catalysts. *Catal. Sci. Technol.* **2014**, *4*, 2814. [[CrossRef](#)]
16. Zhang, Z.; Wang, X.; Zhang, Y.; Lu, S.; Huang, Z.; Huang, X.; Wang, Y. Ambient air benzene at background sites in China's most developed coastal regions: Exposure levels, source implications and health risks. *Sci. Total Environ.* **2015**, *511*, 792–800. [[CrossRef](#)]
17. Li, W.B.; Wang, J.X.; Gong, H. Catalytic combustion of VOCs on non-noble metal catalysts. *Catal. Today* **2009**, *148*, 81–87. [[CrossRef](#)]
18. Lahousse, C.; Bernier, A.; Grange, P.; Delmon, B.; Papaefthimiou, P.; Ioannides, T.; Verykios, X. Evaluation of gamma-MnO₂ as a VOC removal catalyst: Comparison with a noble metal catalyst. *J. Catal.* **1998**, *178*, 214–225. [[CrossRef](#)]
19. Cuo, Z.; Deng, Y.; Li, W.; Peng, S.; Zhao, F.; Liu, H.; Chen, Y. Monolithic Mn/Ce-based catalyst of fibrous ceramic membrane for complete oxidation of benzene. *Appl. Surf. Sci.* **2018**, *456*, 594–601. [[CrossRef](#)]
20. Wang, X.; Kang, Q.; Li, D. Low-temperature catalytic combustion of chlorobenzene over MnO_x-CeO₂ mixed oxide catalysts. *Catal. Commun.* **2008**, *9*, 2158–2162. [[CrossRef](#)]
21. Mo, S.; Li, S.; Li, J.; Peng, S.; Chen, J.; Chen, Y. Promotional effects of Ce on the activity of MnAl oxide catalysts derived from hydrotalcites for low temperature benzene oxidation. *Catal. Commun.* **2016**, *87*, 102–105. [[CrossRef](#)]
22. Yi, H.; Huang, Y.; Tang, X.; Zhao, S.; Gao, F.; Wang, J.; Yang, Z. Improving the Efficiency of Mn-CeO_x/Cordierite Catalysts for Nonmethane Hydrocarbon Oxidation in Cooking Oil Fumes. *Ind. Eng. Chem. Res.* **2018**, *57*, 4186–4194. [[CrossRef](#)]
23. Kim, S.C.; Shim, W.G. Catalytic combustion of VOCs over a series of manganese oxide catalysts. *Appl. Catal. Environ.* **2010**, *98*, 180–185. [[CrossRef](#)]
24. Li, D.; Li, W.; Deng, Y.; Wu, X.; Han, N.; Chen, Y. Effective Ti Doping of δ-MnO₂ via Anion Route for Highly Active Catalytic Combustion of Benzene. *J. Phys. Chem.* **2016**, *120*, 10275–10282. [[CrossRef](#)]
25. Tang, W.; Yao, M.; Deng, Y.; Li, X.; Han, N.; Wu, X.; Chen, Y. Decoration of one-dimensional MnO₂ with Co₃O₄ nanoparticles: A heterogeneous interface for remarkably promoting catalytic oxidation activity. *Chem. Eng. J.* **2016**, *306*, 709–718. [[CrossRef](#)]
26. Trovarelli, A. Catalytic Properties of Ceria and CeO₂-Containing Materials. *Catal. Rev.* **1996**, *38*, 439–520. [[CrossRef](#)]
27. Qiao, Z.; Wu, Z.; Dai, S. Shape-Controlled Ceria-based Nanostructures for Catalysis Applications. *ChemSusChem.* **2013**, *6*, 1821–1833. [[CrossRef](#)]

28. Deng, L.; Ding, Y.; Duan, B.; Chen, Y.; Li, P.; Zhu, S.; Shen, S. Catalytic deep combustion characteristics of benzene over cobalt doped Mn-Ce solid solution catalysts at lower temperatures. *Mol. Catal.* **2018**, *446*, 72–80. [[CrossRef](#)]
29. Kan, J.; Deng, L.; Li, B.; Huang, Q.; Zhu, S.; Shen, S.; Chen, Y. Performance of co-doped Mn-Ce catalysts supported on cordierite for low concentration chlorobenzene oxidation. *Appl. Catal. Gen.* **2017**, *530*, 21–29. [[CrossRef](#)]
30. Azalim, S.; Brahmi, R.; Agunaou, M.; Beaurain, A.; Giraudon, J.M.; Lamonier, J.F. Washcoating of cordierite honeycomb with Ce–Zr–Mn mixed oxides for VOC catalytic oxidation. *Chem. Eng. J.* **2013**, *223*, 536–546. [[CrossRef](#)]
31. Bilal, Y.; Nasir, M.A.; Nasreen, S.; Akhter, N.; Pasha, R.A.; Noor, M.F. Synthesis and Activity Evaluation of Ce-Mn-Cu Mixed Oxide Catalyst for Selective Oxidation of CO in Automobile Engine Exhaust: Effect of Ce/Mn Loading Content on Catalytic Activity. *Adv. Sci. Technol. Res. J.* **2018**, *12*, 260–266. [[CrossRef](#)]
32. He, C.; Yu, Y.; Shi, J.; Shen, Q.; Chen, J.; Liu, H. Mesoporous Cu–Mn–Ce–O composites with homogeneous bulk composition for chlorobenzene removal: Catalytic performance and microactivation course. *Mater. Chem. Phys.* **2015**, *157*, 87–100. [[CrossRef](#)]
33. Zhang, X.; Wu, D. Ceramic monolith supported Mn–Ce–M ternary mixed-oxide (M=Cu, Ni or Co) catalyst for VOCs catalytic oxidation. *Ceram. Int.* **2016**, *42*, 16563–16570. [[CrossRef](#)]
34. Piumetti, M.; Bensaid, S.; Andana, T.; Russo, N.; Pirone, R.; Fino, D. Cerium-copper oxides prepared by solution combustion synthesis for total oxidation reactions: From powder catalysts to structured reactors. *Appl. Catal. Environ.* **2017**, *205*, 455–468. [[CrossRef](#)]
35. Ye, Z.; Giraudon, J.M.; Nuns, N.; Simon, P.; De Geyter, N.; Morent, R.; Lamonier, J.F. Influence of the preparation method on the activity of copper-manganese oxides for toluene total oxidation. *Appl. Catal. Environ.* **2018**, *223*, 154–166. [[CrossRef](#)]
36. Avila, P.; Montes, M.; Miró, E.E. Monolithic reactors for environmental applications. *Chem. Eng. J.* **2005**, *109*, 11–36. [[CrossRef](#)]
37. Govender, S.; Friedrich, H. Monoliths: A Review of the Basics, Preparation Methods and Their Relevance to Oxidation. *Catalysts* **2017**, *7*, 62. [[CrossRef](#)]
38. Liu, G.; Li, J.; Yang, K.; Tang, W.; Liu, H.; Yang, J.; Yue, R.; Chen, Y. Effects of cerium incorporation on the catalytic oxidation of benzene over flame-made perovskite $\text{La}_{1-x}\text{Ce}_x\text{MnO}_3$ catalysts. *Particuology* **2015**, *19*, 60–68. [[CrossRef](#)]
39. Mo, S.; Li, S.; Li, W.; Li, J.; Chen, J.; Chen, Y. Excellent low temperature performance for total benzene oxidation over mesoporous CoMnAl composited oxides from hydrotalcites. *J. Mater. Chem.* **2016**, *4*, 8113–8122. [[CrossRef](#)]
40. Wang, Z.; Shen, G.; Li, J.; Liu, H.; Wang, Q.; Chen, Y. Catalytic removal of benzene over $\text{CeO}_2\text{-MnO}_x$ composite oxides prepared by hydrothermal method. *Appl. Catal. Environ.* **2013**, *138–139*, 253–259. [[CrossRef](#)]
41. Xu, H.; Zhang, Q.; Qiu, C.; Lin, T.; Gong, M.; Chen, Y. Tungsten modified $\text{MnO}_x\text{-CeO}_2/\text{ZrO}_2$ monolith catalysts for selective catalytic reduction of NO_x with ammonia. *Chem. Eng. Sci.* **2012**, *76*, 120–128. [[CrossRef](#)]
42. Tang, W.; Wu, X.; Li, S.; Shan, X.; Liu, G.; Chen, Y. Co-nanocasting synthesis of mesoporous Cu–Mn composite oxides and their promoted catalytic activities for gaseous benzene removal. *Appl. Catal. Environ.* **2015**, *162*, 110–121. [[CrossRef](#)]
43. Wang, Y.; Yang, D.; Li, S.; Zhang, L.; Zheng, G.; Guo, L. Layered copper manganese oxide for the efficient catalytic CO and VOCs oxidation. *Chem. Eng. J.* **2019**, *357*, 258–268. [[CrossRef](#)]
44. Li, B.; Chen, Y.; Li, L.; Kan, J.; He, S.; Yang, B.; Shen, S.; Zhu, S. Reaction kinetics and mechanism of benzene combustion over the $\text{NiMnO}_3/\text{CeO}_2/\text{Cordierite}$ catalyst. *J. Mol. Catal. A Chem.* **2016**, *415*, 160–167. [[CrossRef](#)]
45. He, C.; Liu, X.; Shi, J.; Ma, C.; Pan, H.; Li, G. Anionic starch-induced Cu-based composite with flake-like mesostructure for gas-phase propanal efficient removal. *J. Colloid Interface Sci.* **2015**, *454*, 216–225. [[CrossRef](#)] [[PubMed](#)]
46. Zhao, F.; Li, S.; Wu, X.; Yue, R.; Li, W.; Chen, Y. Synergetic effect over flame-made manganese doped CuO-CeO_2 nanocatalyst for enhanced CO oxidation performance. *RSC Adv.* **2019**, *9*, 2343–2352. [[CrossRef](#)]
47. Delimaris, D.; Ioannides, T. VOC oxidation over CuO-CeO_2 catalysts prepared by a combustion method. *Appl. Catal. Environ.* **2009**, *89*, 295–302. [[CrossRef](#)]

48. Kondrat, S.A.; Davies, T.E.; Zu, Z.; Boldrin, P.; Bartley, J.K.; Carley, A.F.; Taylor, S.H.; Rosseinsky, M.J.; Hutchings, G.J. The effect of heat treatment on phase formation of copper manganese oxide: Influence on catalytic activity for ambient temperature carbon monoxide oxidation. *J. Catal.* **2011**, *281*, 279–289. [[CrossRef](#)]
49. He, C.; Yu, Y.; Shen, Q.; Chen, J.; Qiao, N. Catalytic behavior and synergistic effect of nanostructured mesoporous CuO-MnO_x-CeO₂ catalysts for chlorobenzene destruction. *Appl. Surf. Sci.* **2014**, *297*, 59–69. [[CrossRef](#)]
50. Aguilera, D.A.; Perez, A.; Molina, R.; Moreno, S. Cu–Mn and Co–Mn catalysts synthesized from hydrotalcites and their use in the oxidation of VOCs. *Appl. Catal. Environ.* **2011**, *104*, 144–150. [[CrossRef](#)]



© 2019 by the authors. Licensee MDPI, Basel, Switzerland. This article is an open access article distributed under the terms and conditions of the Creative Commons Attribution (CC BY) license (<http://creativecommons.org/licenses/by/4.0/>).